

Non-linear vortex dynamics in the mixed state of superconducting a -MoGe and NbN thin films using low-frequency two-coil mutual inductance technique

Somak Basistha¹, Soumyajit Mandal, John Jesudasan, Vivas Bagwe and Pratap Raychaudhuri
Tata Institute of Fundamental Research, Homi Bhabha Road, Mumbai 400005, India

Abstract

We use a two-coil mutual inductance technique to investigate the non-linear response of the vortex lattice of two type-II superconducting thin films, namely a very weakly pinned amorphous Molybdenum Germanium (a -MoGe) and a moderate-to-strongly pinned Niobium Nitride (NbN). We observe a strong dependence of the magnetic shielding response of the superconductors on the ac excitation amplitude in the primary coil of the two-coil setup. The sample response is studied through the evolution of the radial profile of the induced current density with increasing drive amplitude, which gets significantly modified by the effect of flux creep. We develop a computation scheme where we iteratively combine the coupled Maxwell-London equations for the geometry of the two coils and the sample involved, with a model developed by Coffey and Clem, to analyze the non-linear ac response. The central result of this analysis is that the effect of flux creep gives rise to a strong nonlinearity in the electrodynamic response in the vortex state of the superconducting thin films, that extends down to very low amplitudes of ac excitation. Our results also show that at subcritical low frequency ac drives, the vortex viscosity is exponentially larger than the Bardeen-Stephen estimate. We present a simple scheme to obtain the intrinsic value of the pinning force constant, which otherwise gets affected due to flux creep even at very low ac drives and point out some outstanding issues that need to be addressed in future theoretical and experimental studies.

¹ Email: somak.b.94@gmail.com

1. Introduction

When a type II superconductor is subjected to a magnetic field greater than its lower critical field H_{c1} , the field penetrates inside the superconductor in the form of quantised flux tubes each carrying a flux of $\phi_0 = \frac{h}{2e}$ Wb, called vortices¹. When an external current is passed through the superconductor, each vortex experiences a Lorentz force, $F_L = \phi_0 \mathbf{J} \times \hat{\mathbf{n}}$, where \mathbf{J} is the current density and $\hat{\mathbf{n}}$ the unit vector along the magnetic field. In a perfectly clean superconductor, this results in the movement of the vortices, which gives rise to dissipation. This dissipation gives rise to an effective viscous force, $-\eta \mathbf{u}$, where \mathbf{u} is the position of the vortex and η is the viscous drag coefficient which can be estimated from the upper critical field, H_{c2} ¹ and the normal state resistivity, ρ_N , using the Bardeen-Stephen model² as, $\eta = \frac{\mu_0 H_{c2} \phi_0}{\rho_N}$. η can be recast as $\eta = \frac{B \phi_0}{\rho_{ff}}$ where B is the applied dc magnetic field and ρ_{ff} is the resistivity in the flux flow regime² of the superconductor, where the velocity of vortices, across the superconductor, is only limited by the viscous drag. In real superconductors, defects in the solid act as potential wells that pin the vortices, thereby altering this behaviour. In the presence of a dc current, dissipation occurs only above a finite critical current density³ (J_c), at which the Lorentz force (F_L) can overcome the pinning force. The situation is more complex under an oscillatory drive, like an ac current or ac magnetic field. Here each vortex can undergo small oscillatory motion within the pinning potential even when $|\mathbf{J}| < J_c$, leading to dissipation. The dynamics of vortices is determined by the interplay of the viscous force and the restoring pinning force. Understanding the dynamics of vortices is therefore of paramount importance both from a fundamental standpoint and from the aspect of technological applications^{4,5,6,7,8,9}.

The two-coil mutual inductance technique^{10,11,12,13,14} is a simple, yet elegant method to investigate the low-frequency electrodynamics of superconducting films, in frequency range

of tens of kHz . In this technique, the superconducting thin film is sandwiched between a primary and a secondary coil such that the film partially shields the magnetic field produced by the primary coil, from the secondary. The electrodynamic response of the superconductor is obtained from the complex mutual inductance ($M = M' + iM''$) between the two coils. This technique has widely been used to measure the penetration depth in superconducting films and to study the Berezinski-Kosterlitz-Thouless transition in ultrathin films¹⁵. Recently¹⁶, this technique was extended to study the electrodynamic response in the vortex state of NbN and α -MoGe superconducting films under a low frequency subcritical ac drive (tens of kHz frequencies). These results showed that for a subcritical kHz drive the vortex viscosity η exceeds the Bardeen-Stephen estimate by several orders of magnitude. Although there are some theories predicting such an enhancement of vortex viscosity, like vortex-pin (Vinokur *et.al*¹⁷), vortex-vortex interactions (Carruzzo *et.al*¹⁸) and more recently, inelastic relaxation of quasiparticles in the vortex core (Pashinsky *et.al*¹⁹) the precise origin of this large enhancement is still debated.

Two-coil measurements are typically performed with very small ac excitations where the response of the superconductor is assumed to be in the linear regime. This assumption is valid typically when the induced current density, J , in the superconductor is much smaller than the critical current density J_c , for example in zero field for most superconductors. On the other hand, in the presence of vortices, processes such thermally activated flux flow (TAFF) and flux creep (FC) can significantly reduce the range of the ac excitation amplitude over which the superconductor is in the regime of linear response. Therefore, it is extremely important to understand the non-linear response of the superconductor to interpret the data. Previous studies on the low frequency ac non-linear response of vortex dynamics using ac susceptibility measurements^{20,21,22,23,24}, have focussed on the hysteretic regime of the superconductor^{25,26}. On the other hand, these studies did not investigate of the non-linear ac response in the non-

hysteretic regime and its implications on the vortex parameters pertaining to the non-linear ac response.

In this paper, we investigate the non-linear electrodynamic response in the vortex state of two superconductors, namely, a 20 nm thick *a*-MoGe thin film with very weak pinning and a moderate-to-strongly pinned NbN thin film of thickness 5 nm. In both samples, we observe a strong dependence of M on the amplitude of the ac drive in the primary coil that persist much above the magnetic field where the hysteresis loop closes. We develop a computation scheme to analyze the data in the non-linear regime and observe that the effect of flux creep plays a major role in the non-linear response of the vortex state, even at very low amplitudes of the ac drive, in the non-hysteretic regime.

2. Theoretical background

Vortices in type-II superconductors, under small oscillatory excitations, behave like forced-damped harmonic oscillators. They are influenced by three forces: (i) the viscous drag force, (ii) the restoring force due to the combined effect of pinning and inter-vortex interactions and (iii) the Lorentz force due to the oscillatory current. Gittleman and Rosenblum's²⁷ (GR) model describes vortex dynamics for a single vortex, neglecting vortex mass term and thermal effects. Under these approximations the equation of motion of the vortex is given by:

$$\eta \dot{\mathbf{u}} + \alpha \mathbf{u} = \phi_0 \mathbf{J}^{ac} \times \hat{\mathbf{n}} \quad (1)$$

\mathbf{J}^{ac} is the ac drive current density, $\hat{\mathbf{n}}$ is the unit vector along the magnetic field of the vortex, η is the viscous drag coefficient of the vortices in absence of pinning and flux creep, and α is the restoring force constant (Labusch parameter²⁸) of the vortex. It is a mean-field model²⁹, which captures the vortex dynamics if the thermally activated motion of the vortices is slow compared

to the excitation frequency. For a harmonic solution ($\sim e^{i\omega t}$) of eqn. (1), we get $\mathbf{u} = \phi_0 \frac{\mathbf{J}^{ac} \times \hat{\mathbf{n}}}{(\alpha + i\omega\eta)}$. This value when substituted into the London equation³⁰ we get²⁹:

$$\mathbf{A} = -\mu_0 \lambda_L^2 \mathbf{J}^{ac} + \mathbf{u} \times \mathbf{B} = -\mu_0 \left(\lambda_L^2 + \frac{\phi_0 B}{\mu_0 (\alpha + i\omega\eta)} \right) \mathbf{J}^{ac} = -\mu_0 \tilde{\lambda}^2 \mathbf{J}^{ac} \quad (2)$$

Eqn. (2) assumes a form similar to the usual London equation, where the London penetration depth³¹ (λ_L) is replaced by the effective complex penetration depth, $\tilde{\lambda}$. The term $\frac{\phi_0 B}{\mu_0 (\alpha + i\omega\eta)}$ captures the effect of the pinning force and viscous drag, and in the low frequency limit, $\omega \ll \alpha/\eta$, reduces to the square of the well-known Campbell penetration depth^{32,33,34} given by, $\lambda_C = \left(\frac{\phi_0 B}{\mu_0 \alpha} \right)^{1/2}$. It is often useful to rewrite $\tilde{\lambda}^2$ in terms of the complex vortex resistivity, ρ_v :

$$\tilde{\lambda}^2 = \lambda_L^2 + \frac{\phi_0 B}{\mu_0 (\alpha + i\omega\eta)} = \lambda_L^2 + \frac{\lambda_C^2}{(1 + i\omega\tau_0)} = \lambda_L^2 - \frac{i \rho_v}{\mu_0 \omega} \quad (3)$$

where $\tau_0 = \eta/\alpha$ is the vortex relaxation time and ρ_v is expressed in terms of dc flux flow resistivity (ρ_{ff}) as^{29,30}: $\rho_v = \rho_{ff} \frac{i\omega\tau_0}{1 + i\omega\tau_0}$; $\rho_{ff} = \frac{B\phi_0}{\eta} = \frac{B}{B_{c2}} \rho_n$, where ρ_n is the normal state resistivity.

Eqn. (2) does not take thermal effects into consideration. At finite temperatures, the strength of the pinning barriers being finite, there is a finite probability of the vortices to hop from one pinning site to another neighbouring pinning site, owing to their thermal energy. In the absence of any external drive, these hops have no preferential direction and hence there is no net motion of the vortices. This process, called thermally activated flux flow (TAFF), has the effect of relaxing the restoring pinning force over characteristic time scale of vortex hop. This effect becomes particularly important when measurements are done at low frequencies. We use a model proposed by Coffey and Clem³⁵ (CC model), who added a random Langevin force, dependent on the effective pinning potential barrier (U), to simulate the thermal motion and then solve it similar to that of a particle undergoing Brownian motion in a periodic

potential^{36,37}. This leads to a modification of eqn. (3), where the complex resistivity takes the form³⁸,

$$\rho_v \rightarrow \rho_v^{TAFF} = \rho_{ff} \frac{\epsilon + i\omega\tau}{1 + i\omega\tau} \quad (4)$$

where τ is the relaxation rate and ϵ is a dimensionless parameter which is a measure of the weight of the TAFF phenomenon. They are given as:

$$\epsilon = \frac{1}{I_0^2(\nu)} \quad (5 \text{ (a)})$$

$$\tau = \tau_0 \frac{I_0^2(\nu) - 1}{I_1(\nu)I_0(\nu)} \quad (5 \text{ (b)})$$

where $\nu = \frac{U}{2k_B T}$ and I_0 and I_1 are the zeroth and first order modified Bessel functions of the first kind. Consequently, CC model has three temperature dependent parameters, α , η and U . Furthermore, the normal skin depth (δ_{nf}) arising from the electrodynamic response of the normal electrons introduces an additional correction such that eqn. (3) is modified into:

$$\tilde{\lambda}^2 = \left(\lambda_L^2 - i \frac{\rho_v^{TAFF}}{\mu_0 \omega} \right) / \left(1 + 2i \frac{\lambda_L^2}{\delta_{nf}^2} \right) \quad (6)$$

Here, δ_{nf} has the phenomenological variation of the form $\sim \left(\frac{(\frac{2\rho_n}{\mu_0\omega})}{1-f(t,h)} \right)^{1/2}$ which is

complementary to the variation of λ_L , where $\lambda_L^2(t,h) = \frac{\lambda_L^2}{f(t,h)}$, both of which comes from analysing a superconductor in the framework of the two-fluid model. Here ρ_n is the normal state resistivity and $f(t,h) = (1-t^4)(1-h)^{35,30}$ with $t = T/T_c$ and $h = H/H_{c2}(t)$.

Since, $\lambda_L \sim 361 \text{ nm}$ for NbN and 588 nm for *a*-MoGe¹⁶, $\frac{2\lambda_L^2}{\delta_{nf}^2} \ll 1$ and hence we can drop the this term from the denominator of eqn. (6).

Apart from TAFF, there is another motion that the vortices exhibit, called flux creep³⁰. When an external drive in the form of a current density (\mathbf{J}) is present, the Lorentz force density ($\sim \mathbf{J} \times \mathbf{B}$) acts on the vortices and the original pinning potential becomes a tilted washboard model, which introduces a difference in the rate of forward (in the direction of the Lorentz force) hopping and backward (against the direction of the Lorentz force) hopping. Flux creep has the effect of reducing U . Kim and Anderson^{39,40} first worked out this phenomenon, where the effective pinning potential gets attenuated by the external drive and is given by: $U(J) \sim U_0 \left(1 - \frac{|J|}{J_{c0}}\right)$, where J_{c0} is the critical current density without flux creep. However later works by Beasley⁴¹ and more recent works by Griessen⁴² and Lairson⁴³ showed that this expression gets modified to:

$$U(J) \sim U_0 \left(1 - \frac{|J|}{J_{c0}}\right)^{3/2} \quad (7)$$

when the anharmonicity of the pinning potential is taken into consideration. In the regime of $J \ll J_{c0}$, an inverse power law barrier (Feigel'man *et al.*^{44,45}):

$$U(J) \sim U_c \frac{\left[\left(\frac{J_{c0}}{|J|}\right)^\mu - 1\right]}{\mu} \quad (8)$$

and a logarithmic barrier (Zeldov *et al.*^{46,47})

$$U(J) \sim U_c \ln \left(\frac{J_{c0}}{|J|}\right) \quad (9)$$

has been used to study flux creep in high temperature superconductors, mostly in the regime of collective creep in vortex solids.

Apart from the reduction in U , the effect of flux creep also results in J dependence of α and η . Prozorov *et al.*⁴⁸ showed that, considering a cubic anharmonicity of the pinning potential, α gets modified as

$$\alpha(J) \sim \alpha_0 \left(1 - \frac{|J|}{J_{c0}}\right)^{1/2} \quad (10)$$

Within the tilted washboard model this functional form is derived from the local curvature of the pinning potential at the new equilibrium position of the vortex in the presence of a current density. On the other hand, the J dependence of vortex viscosity η comes from the J dependence of U . It has been suggested that η gets enhanced due to vortex-vortex and vortex-pin interactions. Vinokur *et al.*¹⁷ and Carruzzo *et al.*¹⁸ introduced an empirical form of this enhanced η , which is given by:

$$\eta(J) \sim \eta_{BS} e^{U(J)/k_B T} \quad (11)$$

where η_{BS} is the BS viscosity. Qualitatively, this functional form predicts that η will exceed the Bardeen-Stephen value at subcritical current and reach the Bardeen-Stephen limiting value for $J \geq J_c$.

The final form of the CC equation that we use is:

$$\begin{aligned} \tilde{\lambda}^{-2} &= \lambda^{-2} + i\delta^{-2} = \left(\lambda_L^2 - i \frac{\rho_{ff}}{\mu_0 \omega} \frac{\epsilon + i\omega\tau}{1 + i\omega\tau} \right)^{-1} \\ &= \left(\lambda_L^2 - \frac{\rho_{ff}}{\mu_0 \omega (1 + (\omega\tau)^2)} (\omega\tau(\epsilon - 1) + i(\epsilon + (\omega\tau)^2)) \right)^{-1} \end{aligned} \quad (12)$$

Here, λ accounts for the inductive response, while δ measures the dissipative response of the superconductor. In this work, we use eqn. (12) along with eqns. (7), (10) and (11) to address the non-linear response of the vortex state, which arises from the J dependence of U , α and η .

3. Sample and Experimental Details

Sample details: The samples under investigation are a 20 nm thick superconducting *a*-MoGe thin film and a 5 nm thick superconducting NbN thin film, both grown on a (100) MgO

substrate, using pulsed laser deposition and dc magnetron sputtering respectively. Details of sample growth and characterisation can be found in refs. [49], [50] and [51]. The T_c determined from the two-coil mutual inductance response (fig. 1) is 7 K for a -MoGe film and 12 K for NbN film respectively. Furthermore, for both films M' shows a sharp drop whereas M'' shows a narrow single peak just below T_c , confirming the homogeneous nature of our films.

The contrasting pinning properties of the two samples can be seen from the inset of fig.

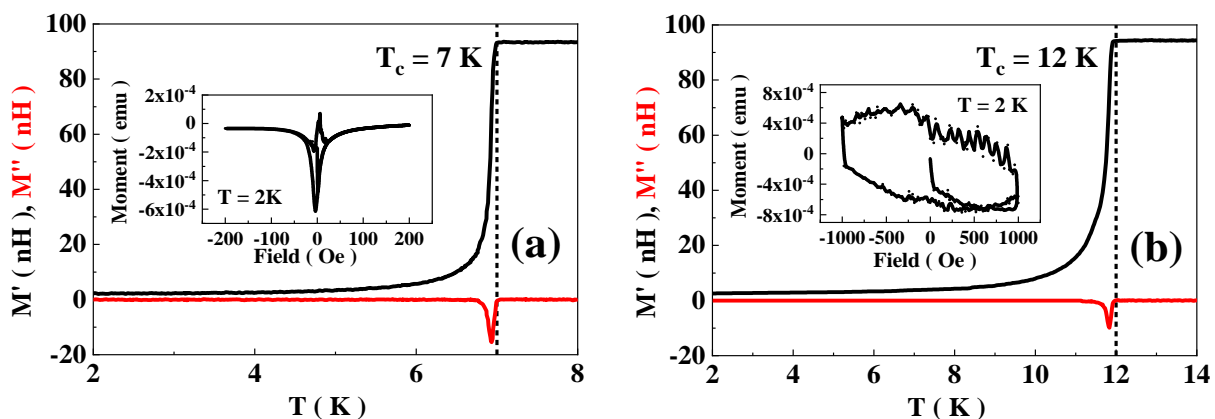


Figure 1. Zero-field temperature variation of M' and M'' for (a) 20 nm thick, superconducting a -MoGe film, and (b) 5 nm thick, superconducting NbN film, both grown on (100) oriented MgO substrates. M' and M'' are plotted as black and red solid lines respectively. The dashed lines correspond to T_c which is ~ 7 K for a -MoGe and ~ 12 K for NbN. These measurements are performed with $I_{ac} \sim 0.05$ mA and $f = 30$ kHz. The insets show variation of magnetic moment as a function of DC magnetic field ($m - H$) loops for the same samples, performed using a SQUID-VSM at $T = 2$ K.

1 (a) and 1 (b) where we plot the magnetisation (m) as a function of an applied DC magnetic field (H) for the two films at 2 K, measured using a SQUID-vibration sample magnetometer (SQUID-VSM). Both samples show hysteresis in $m - H$ typical of a type II superconductor. However, while for NbN the hysteresis loop is considerably open at 1 kOe, for a -MoGe the loop closes around 25 Oe showing its extremely weakly pinned nature. Therefore, in terms of pinning strength these two samples lie on two ends of the spectrum: the NbN film is strongly pinned while the pinning in a -MoGe thin film is extremely weak.

Measurement of the low frequency electrodynamic response: We probe the vortex low

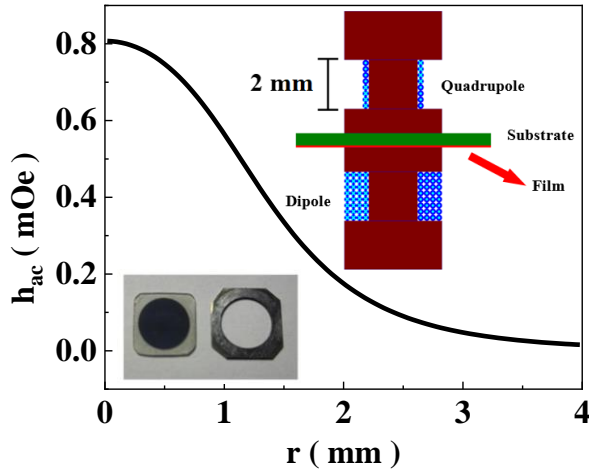


Figure 2. Radial variation of ac field amplitude (I_{ac}) generated across the sample plane from passing 0.05 mA ac excitation through primary quadrupole coil (black); (inset: top right) schematic of the two-coil setup: quadrupole as primary coil (top) and dipole as secondary coil (bottom) with sample sandwiched in between. The coil wire diameter ($50\text{ }\mu\text{m}$) is drawn bigger than the actual for clarity; (inset: bottom left) 8 mm diameter sample grown on MgO substrate (left) using stainless steel mask (right).

frequency dynamics, by measuring the ac shielding response of the superconductor, through measurement of the mutual inductance (M) between the two coils. In this setup^{10,11,12}, we sandwich an 8 mm diameter superconducting thin film, grown using a shadow mask (bottom left inset of fig. 2) in between a miniature quadrupolar primary coil and a dipolar secondary coil. Both the primary and secondary coils are wound on bobbins of 2 mm diameter made from Delrin. An ac current with amplitude I_{ac} and frequency, f ($= 30\text{ kHz}$), is passed through the primary coil and the resulting in-phase (V_{in}) and out-of-phase voltage (V_{out}), in the secondary is measured using a lock-in amplifier. The complex mutual inductance between the two coils is given by $M'(M'') = V_{out}(V_{in}) / (2\pi f I_{ac})$, where M' corresponds to the inductive response and M'' corresponds to the dissipative response.

The schematic of the two-coil setup is given in the top right inset of fig. 2. The quadrupolar primary coil consists of 15 turns clockwise in one half of the coil and another 15 turns counter-clockwise in the other half. The use of a quadrupolar coil ensures fast radial decay of the ac magnetic field on the film, which minimises the effect of edge effects⁵² and geometric^{53,54} barriers. The ac magnetic field (h_{ac}) generated by the primary coil has a maximum (h_p) at the centre of the sample and decreases radially, reaching a value $0.02 h_p$ at the edge of the film. For our coil geometry, h_p/I_{ac} , is 16 Oe/A such that at the maximum

frequency dynamics, by measuring the ac shielding response of the superconductor, through measurement of the mutual inductance (M) between the two coils. In this setup^{10,11,12}, we sandwich an 8 mm diameter superconducting thin film, grown using a shadow mask (bottom left inset of fig. 2) in between a miniature quadrupolar primary coil and a dipolar secondary coil. Both the primary and secondary coils are wound on bobbins of 2 mm diameter made from Delrin. An ac current with amplitude I_{ac} and frequency, f ($= 30\text{ kHz}$), is passed through the primary coil and the resulting in-phase (V_{in}) and out-

drive amplitude of 15 mA , $h_p \sim 240\text{ mOe}$. The dipolar secondary coil consists of 120 turns wound in four layers. Both the coils are made of $50\text{ }\mu\text{m}$ diameter copper wires. We study the amplitude dependent shielding response of the superconducting films at a fixed temperature of 2 K , at an operating frequency of 30 kHz and at different applied dc magnetic fields. We ramp I_{ac} , from 0.05 mA till 6 mA (for $a\text{-MoGe}$) and 15 mA (for NbN). The lower limit of (I_{ac}) is kept at 0.05 mA , as the signal level becomes comparable to the noise threshold below that value. The upper limit of the ac amplitude is chosen based on the magnitude, where M' nears saturation or heating sets in the sample, whichever occurs earlier.

4. Results

In fig. 3, we summarize the ac shielding response of the two superconductors, as a function of the amplitude of ac excitation in the primary coil, at a temperature of 2 K and at different applied dc magnetic fields. The peak of the ac magnetic field, generated on the superconductors, due to passage of the ac excitation is given in the top x-axis of each subplot of fig. 3. We observe with increasing I_{ac} , M' (fig. 3 (a) and (c)) increases monotonically towards the normal state value (94 nH). M'' (fig. 3 (b) and (d)) shows a dissipative peak, which becomes broader with increasing dc magnetic field. For $a\text{-MoGe}$ we restrict the lower value of dc magnetic field to 100 Oe , to stay away from the hysteretic regime as indicated by SQUID measurements. For the same reason, for NbN, the dc magnetic field is restricted down to 2 kOe . A contrasting feature between $a\text{-MoGe}$ and NbN, is that, in NbN, at low fields ($2\text{ kOe} - 20\text{ kOe}$), M' (M'') varies weakly till about $I_{ac} \sim 2\text{ mA}$ and then, a rapid variation sets in. For $a\text{-MoGe}$, there is a steady variation in M' and M'' throughout the entire range of I_{ac} . This difference is owing to the much stronger pinning in the NbN film as compared to $a\text{-MoGe}$ as we will show later.

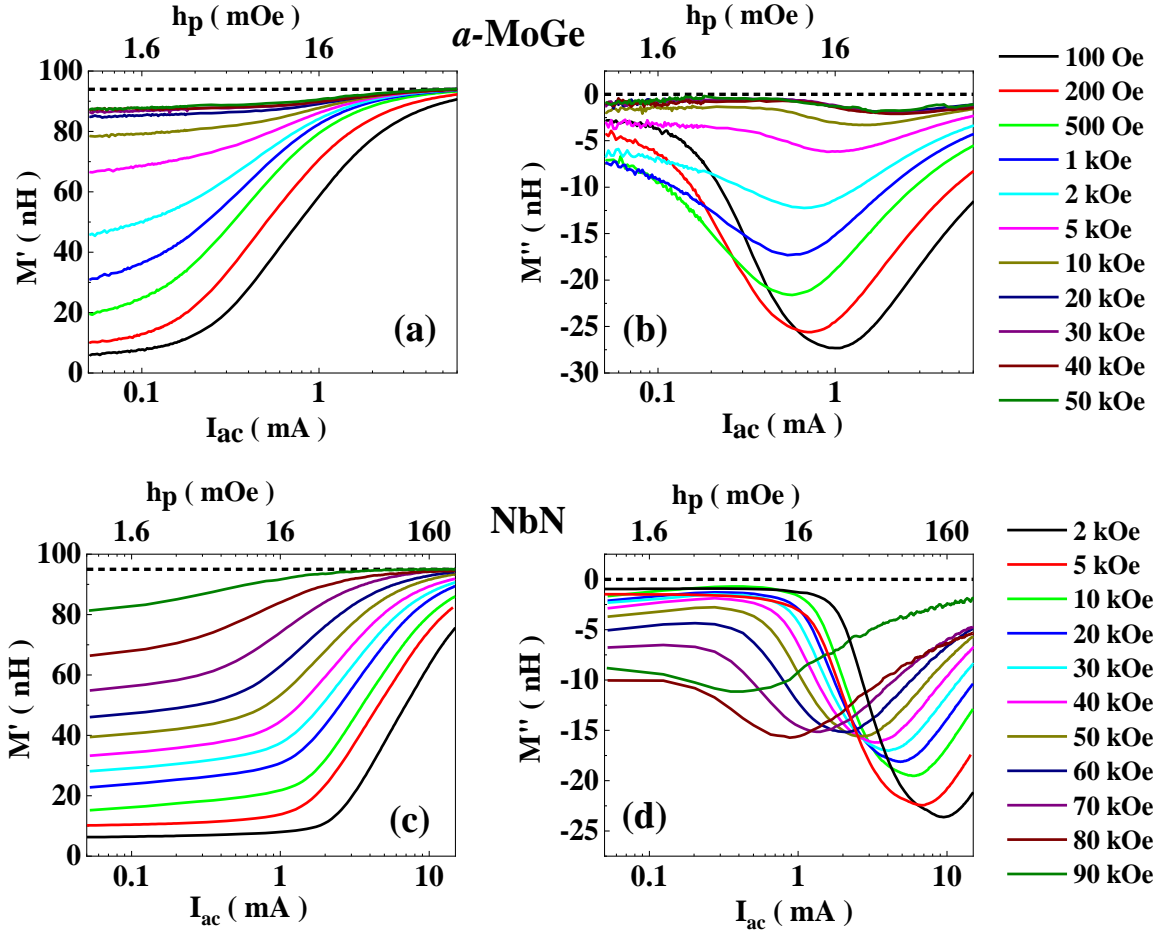


Figure 3. Magnetic field variation of M' and M'' with I_{ac} (bottom x-axis) and the corresponding h_p (top x-axis) produced by the primary coil, for (a) – (b) a -MoGe and (c) – (d) NbN. The dotted lines in black show the M' and M'' value in the normal state, which is 94 nH for M' and 0 nH for M'' . The measurements are done at 2 K and at a frequency of 30 kHz .

5. Discussions

5.1 Effect of ac excitation amplitude on the electromagnetic shielding response of a superconductor

To understand the effect of I_{ac} on the shielding response of a superconducting film, we start by analysing the induced current density in the films due to the magnetic field produced by the primary coil. When I_{ac} is very low, the magnitude of the induced current density (J_{ac}) on the superconducting film, is much smaller than J_c . Therefore, the effect of flux creep on U , α and

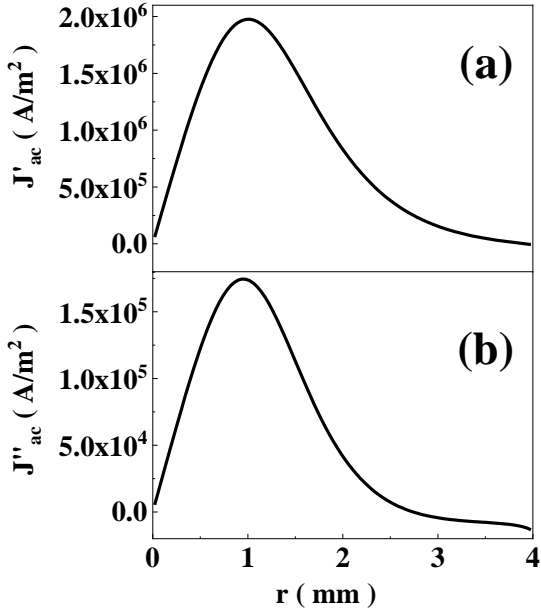


Figure 4. (a) – (b) show the radial profile of the real (J'_{ac}) and imaginary (J''_{ac}) components of the induced current density (J_{ac}) at $I_{ac} = 0.05 \text{ mA}$ without considering the effect of flux creep. We have taken $\lambda = 1890 \text{ nm}$ and $\delta = 6.6 \times 10^6 \text{ nm}$. These values correspond to $\alpha_0 \sim 46 \text{ Nm}^{-2}$, $\frac{U_0}{k_B} \sim 13.2 \text{ K}$ and $\eta = \eta_{BS} e^{U_0/k_B T}$ where $\eta_{BS} \sim 1.47 \times 10^{-8} \text{ Nsm}^{-2}$ at $T = 2 \text{ K}$ and $B = 1 \text{ kOe}$.

η are negligible and $\tilde{\lambda}$ can be taken as a constant. In this regime, we can calculate J_{ac} by numerically solving the coupled Maxwell and London equations using a procedure developed by Turneaure *et al.*^{10,11}. Fig. 4 (a) and (b) shows typical profiles of the real and imaginary part of J_{ac} (J'_{ac} and J''_{ac} respectively).

When the effect of creep is included, $\tilde{\lambda}$ gets locally modified based on the local value of J_{ac} , and therefore $\tilde{\lambda}(J_{ac})$ acquires a radial dependence. This, in turn modifies the radial profile of J_{ac} . To obtain a consistent description of the modified $\tilde{\lambda}$ and J_{ac} due to flux creep for a given value of U_0, α_0 and J_c , we adopt an iterative

procedure. We start by solving the coupled Maxwell-London with a constant $\tilde{\lambda}$, corresponding to the lowest I_{ac} , and obtain a profile for J_{ac} . Next, we use these J_{ac} values, to account for the effect of flux creep on $\tilde{\lambda}$, using eqns. (7), (10), (11) and (12) and obtain $\tilde{\lambda}(r)$. We then use this modified $\tilde{\lambda}(r)$ to recalculate J_{ac} . This procedure is repeated, till a convergence in J_{ac} is achieved. The details of the iterative procedure are given in Appendix A.

Fig. 5 shows the radial variation of J'_{ac} and J''_{ac} , corresponding to a constant $\tilde{\lambda}$, and that obtained after convergence of the iterative procedure discussed above, at four different values of I_{ac} for *a*-MoGe at 1 kOe and 2 K . As expected, with increasing I_{ac} , the effect of flux creep

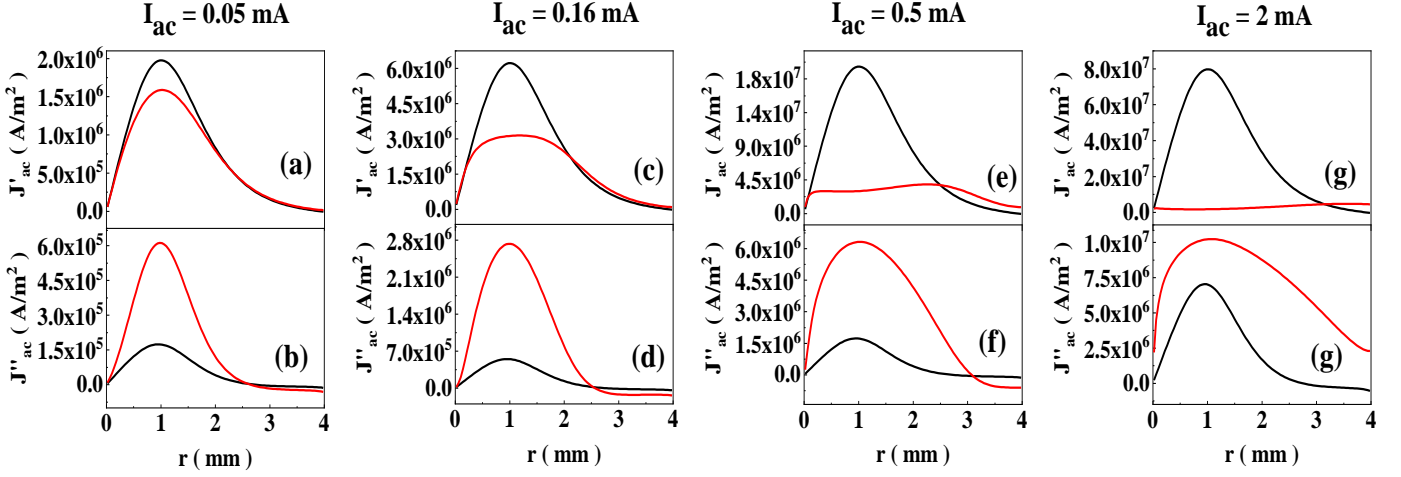


Figure 5. Radial profile of the real (J'_{ac}) and imaginary (J''_{ac}) components of J_{ac} without (black solid lines) and with (red solid lines) the effect of flux creep for (a) – (b) $I_{ac} = 0.05 \text{ mA}$, (c) – (d) $I_{ac} = 0.16 \text{ mA}$, (e) – (f) $I_{ac} = 0.5 \text{ mA}$ and (g) – (h) $I_{ac} = 2 \text{ mA}$. We have taken $\alpha_0 \sim 46 \text{ Nm}^{-2}$, $\frac{U_0}{k_B} \sim 13.2 \text{ K}$ and $J_c \sim 4.8 \times 10^7 \text{ Am}^{-2}$ along with $\eta = \eta_{BS} e^{U_0/k_B T}$ where $\eta_{BS} \sim 1.47 \times 10^{-8} \text{ Nsm}^{-2}$ at $T = 2 \text{ K}$ and $B = 1 \text{ kOe}$.

becomes more prominent. In the profile of J'_{ac} (fig. 5 (a), (c), (e) and (g)), the peak around 1 mm from the sample centre starts to flatten out and at large drive current, there appears a slight dip. This profile can be qualitatively understood from the fact that close to the radius where the bare J'_{ac} is large, the effect of creep is to cause a steep increase in λ ; this acts as negative feedback eventually decreasing J'_{ac} . (These profiles are similar to the ones previously calculated in ref. [55], [56] using a slightly different method). J''_{ac} (fig. 5 (b), (d), (f) and (h)) increases steadily with I_{ac} , and at larger I_{ac} the dissipative response dominates.

To calculate $M'(M'')$ and fit the data, we calculate the combined magnetic field arising from the calculated current profile in the film and the magnetic field produced by the primary coil to find the induced voltage in the secondary coil^{10,11,12}. α_0 , U_0 and J_c are used as adjustable parameters to obtain the best fit to the $M' \text{ vs } I_{ac}$ curve. The evolution of $M'(M'')$ with I_{ac} for $a\text{-MoGe}$ at 1 kOe and 2 K calculated in this way along with the experimental data is shown in fig. 6. We note that this computation technique is successful in qualitatively capturing the

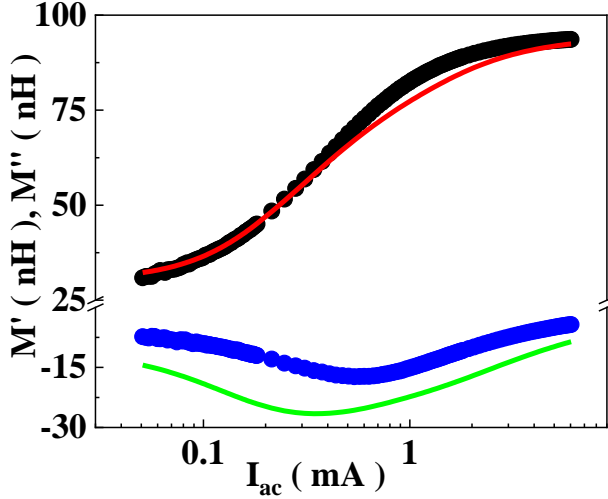


Figure 6. show the AC amplitude dependence of M' and M'' for a -MoGe at 2 K, 1 kOe. The black and blue solid circles represent the experimental data for M' and M'' respectively, while the red and green solid lines represent the fitted response to M' and M'' . The fit parameters are: $\alpha_0 \sim 46 \text{ Nm}^{-2}$, $\frac{U_0}{k_B} \sim 13.2 \text{ K}$ and $J_c \sim 4.8 \times 10^7 \text{ Am}^{-2}$ along with $\eta = \eta_{BS} e^{U_0/k_B T}$ where $\eta_{BS} \sim 1.47 \times 10^{-8} \text{ Nsm}^{-2}$.

variation of M' over the entire range. Quantitatively, the variation of M' is very well captured from low to intermediate I_{ac} , but a small deviation is observed at higher I_{ac} , indicating a breakdown of the perturbative expansions based on which, formulae in eqns. (7), (10) and (11) are derived. On the other hand, for M'' , we capture the qualitative trend, but the calculated value is larger than the measured value. As we will discuss later, that although this analysis largely captures the quantitative variation of M' , there are some serious quantitative disagreements in some current regimes.

5.2 Fits to the magnetic field variation of the electromagnetic shielding response of a -MoGe and NbN

a -MoGe: Fig. 7 (a) – (f) show the fits to the amplitude dependence of M' and M'' for a -MoGe thin film at different applied DC magnetic fields. We observe that the variation of M' with I_{ac} is quantitatively captured, with a small deviation at higher drive amplitudes, while the trend in M'' is captured qualitatively, albeit with an over-estimation. The fits to M' gets better with increasing dc magnetic field. We have used the Beasley model of flux creep in our fitting routine. This model has been used previously while analysing $I - V$ characteristics of a similar film by Buchachek *et al.*⁵⁷. The fits to the complete dataset for a -MoGe is provided in Appendix

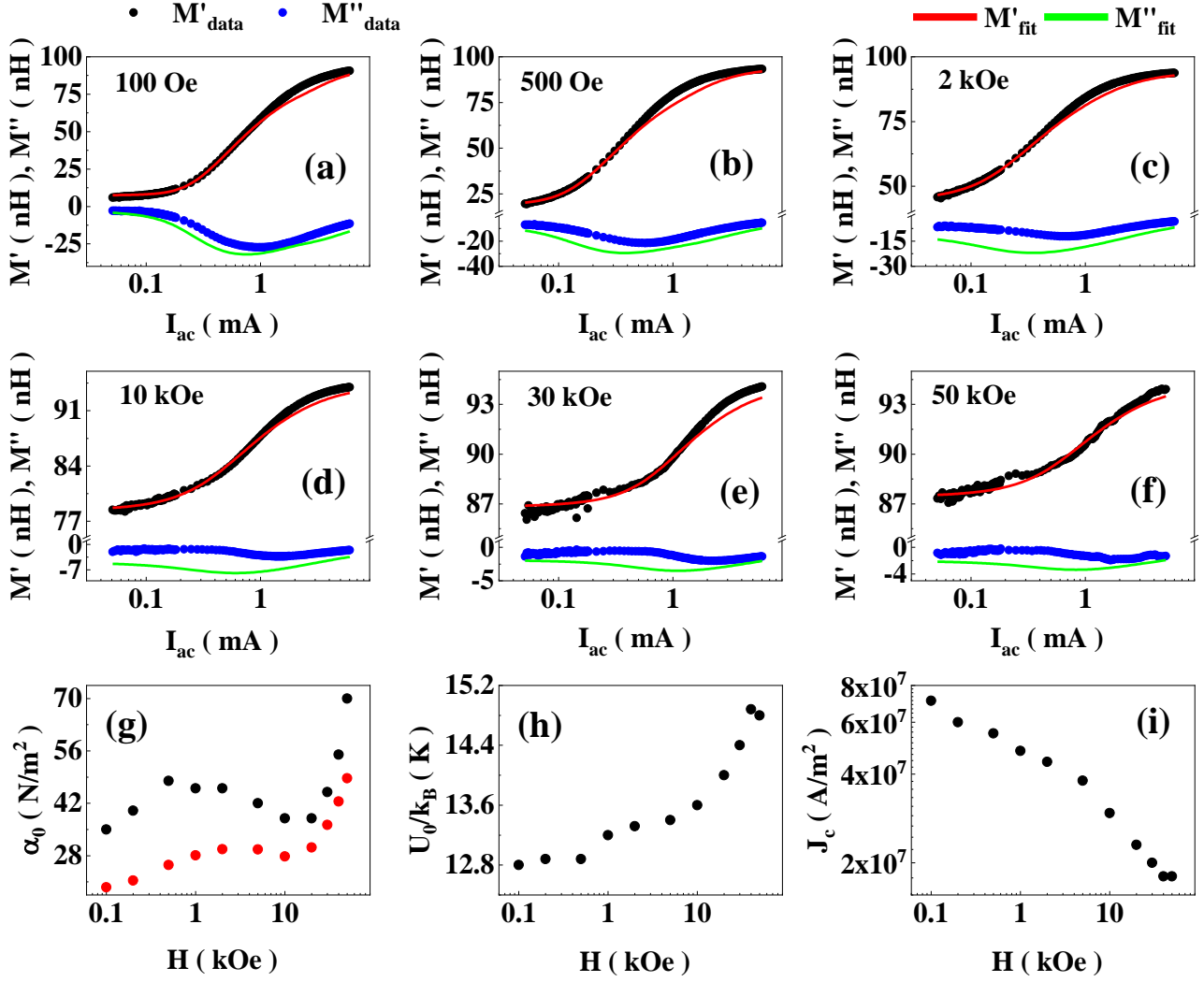


Figure 7. (a) – (f) I_{ac} dependence of M' and M'' of 20 nm *a*-MoGe at different applied DC magnetic fields. The black and blue solid circles are the experimentally measured M' and M'' respectively while the red and green solid lines are the fits to M' and M'' . Magnetic field dependence of (g) α_0 (ref. [16], using GR model, neglecting flux creep, (red solid circles) and this analysis (black solid circles)), (h) $\frac{U_0}{k_B}$ and (i) J_c which are the parameters used for fitting with the Beasley model of flux creep at $T = 2 K$ and $f = 30 kHz$.

B. The variation of α_0 , U_0 , and J_c with magnetic field is shown in fig. 7 (g) – (i). The values of J_c are of the same order of magnitudes as the ones obtained earlier from dc current voltage ($I - V$) measurements on a similar sample⁵⁸. The variation of α_0 follows the same trend as the one obtained from the value of $\tilde{\lambda}$ calculated from M measured at the lowest I_{ac} using the analysis based on the GR model (eqn. (3)) which neglects the effect of flux creep. This is

similar to the analysis done in ref. [16]. However, the absolute values are larger by a factor of 1.5 – 2. We will discuss the origin of this difference later. The magnitude of U_0 also differs from ref. [16], but this is not surprising since in ref. [16] at low temperatures, U_0 was calculated by extrapolating its value close to T_c , thereby introducing large errors.

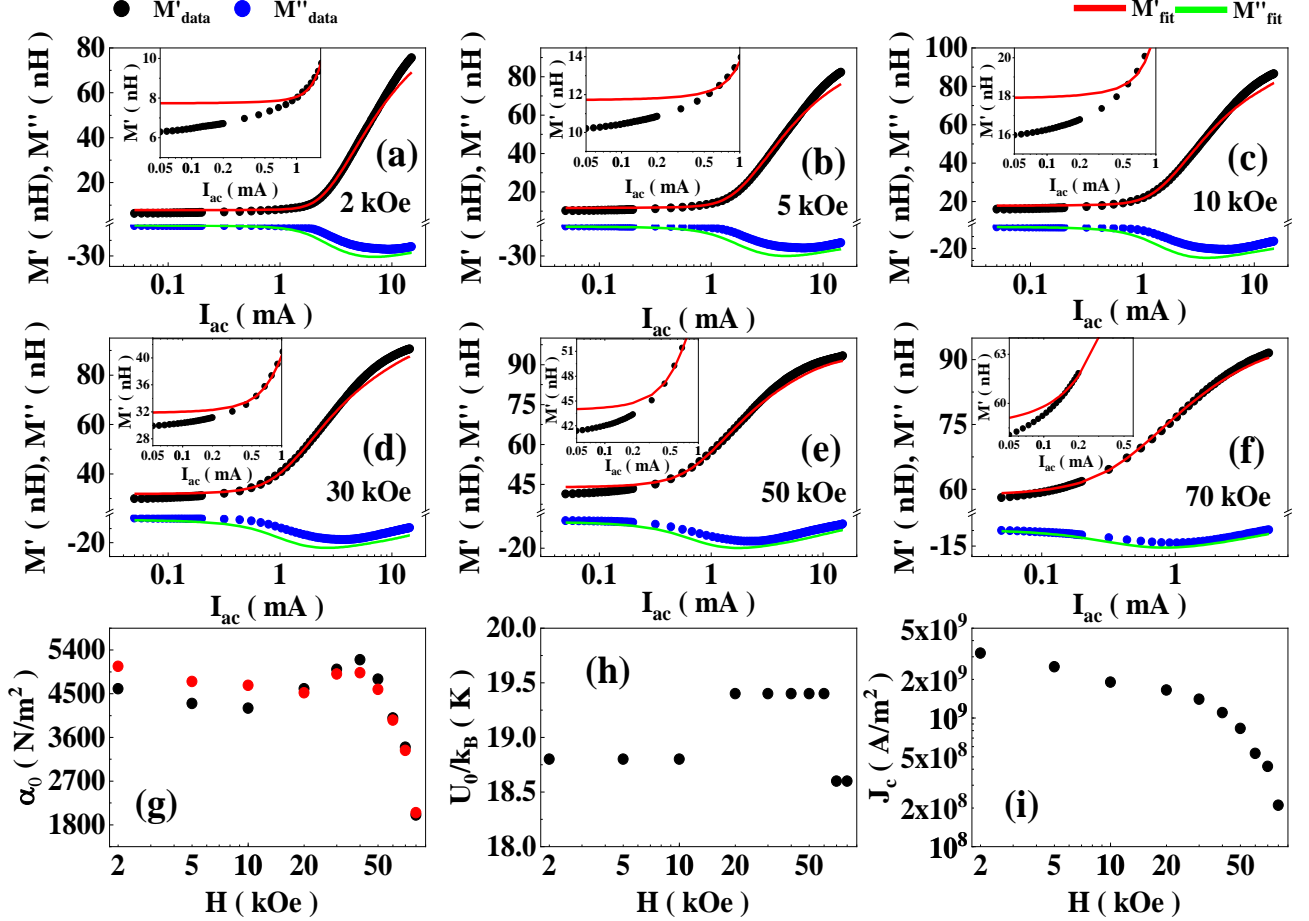


Figure 8. (a) – (f) I_{ac} dependence of M' and M'' of 5 nm NbN at different applied DC magnetic fields. The black and blue solid circles are the experimentally measured M' and M'' respectively while the red and green solid lines are the fits to M' and M'' . The insets show the deviation of the fit to M' from the experimentally measured value, in the low I_{ac} regime. Magnetic field dependence of (g) α_0 , (ref. [16], using GR model, neglecting flux creep, (red solid circles) and this analysis (black solid circles)) (h) $\frac{U_0}{k_B}$ and (i) J_c which are the parameters used for fitting with the Beasley creep model at $T = 2 K$ and $f = 30 kHz$.

NbN: We show the fits to the amplitude dependence of M' and M'' for NbN at different DC magnetic fields in fig. 8 (a) – (f). The Beasley model of flux creep captures the variation in M' quantitatively, with a small deviation at higher I_{ac} . However, in this case at very small I_{ac} ($<$

0.7 mA), we also observe a significant deviation between the fit and the experimental M' , as seen from the expanded views in the insets of fig 8 (a) – (f). The near linear variation of M' in the low I_{ac} regime could not be fitted with any of the existing models of flux creep and needs to be studied further. The overall I_{ac} variation in M'' is captured qualitatively, but with an overestimation, like a -MoGe although at the low I_{ac} and magnetic fields, the fits and the experimental M'' are in very good agreement with each other. The fits to the complete dataset for NbN is provided in Appendix B. Fig 8 (g) – (i) show the magnetic field variation of the fitting parameters: α_0 , U_0 , and J_c respectively. The values of J_c are of the same order of magnitude as the ones obtained from earlier studies on similar samples^{59,60}. The magnitude of α_0 is very close to the one obtained from $\tilde{\lambda}$ calculated from M measured at the lowest I_{ac} using the analysis based on the GR model (eqn. (3)) in ref. [16], since the effect of creep is much less pronounced in NbN than in a -MoGe at low I_{ac} . The difference in the two values is primarily because we cannot capture the variation in M' at low current using the creep models used here. The magnitude of U_0 differs from ref. [16], for the reason similar to a -MoGe.

5.3 Effect of flux creep on the pinning force constant α

We have seen in fig. 7 (g) that for a -MoGe the value of α obtained from analysis of the data at the lowest $I_{ac} \sim 0.05$ mA, differs significantly from the value obtained from the analysis here that includes the effect of flux creep. This comes from the fact that for very weakly pinned superconductors such as the a -MoGe thin film, J_c is small and neglecting the effect of flux creep results in underestimating α .

To elucidate this point, we calculate the apparent Labusch parameter $\tilde{\alpha}$ as a function of I_{ac} from M' and M'' neglecting the effect of flux creep on the current density profile. For this we first invert the experimentally measured M' and M'' using the scheme outlined in ref. [16] to obtain an effective $\tilde{\lambda}$ that is independent of the induced current density. Then using eqn. (3)

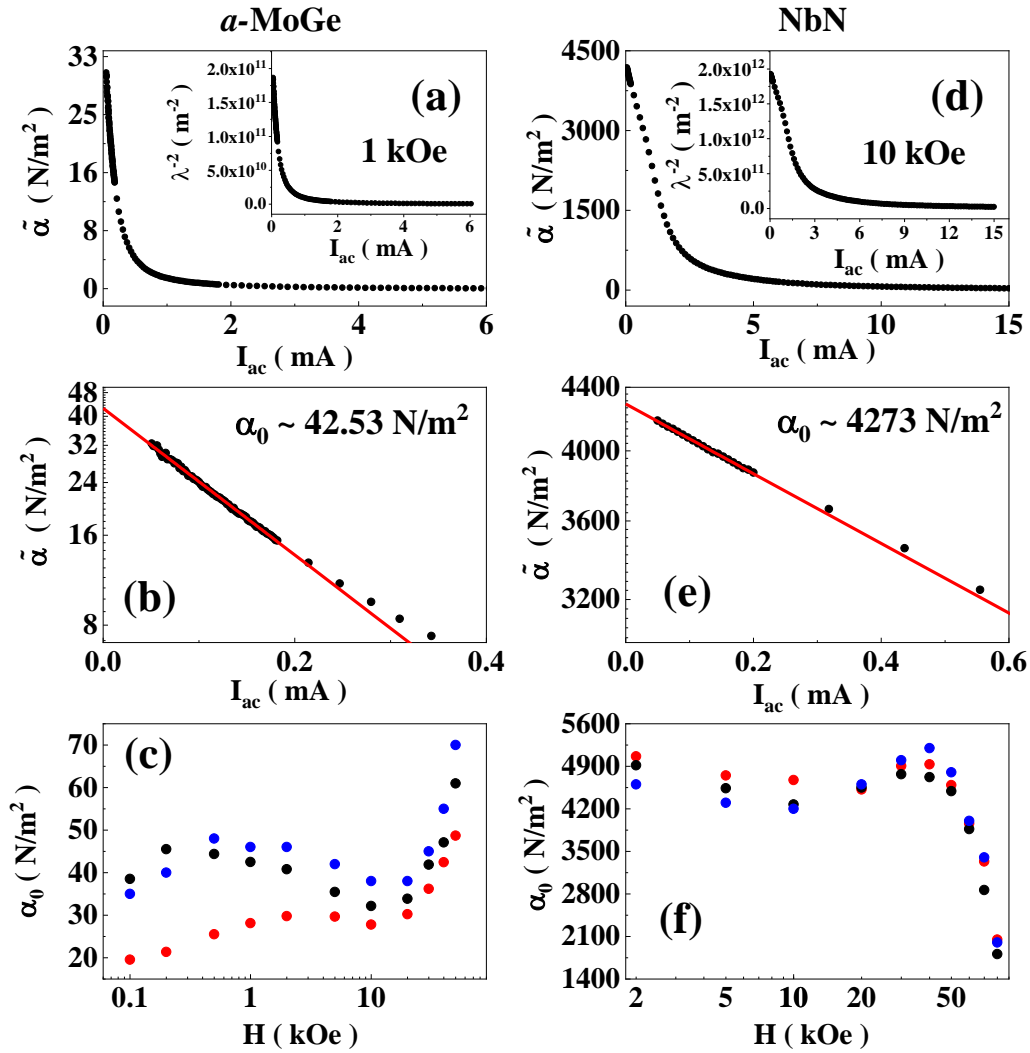


Figure 9. Variation of $\tilde{\alpha}$ with I_{ac} for (a) *a*-MoGe at 1 kOe and (d) NbN at 10 kOe (black solid circles) extracted from λ using the GR model, ignoring flux creep (eqn. (3)). Inset shows the I_{ac} variation of λ^{-2} , calculated by inverting $M'(M'')$ as done in ref. [16]. Expanded view of $\tilde{\alpha}$ vs I_{ac} (black solid circles) in log-linear scale for (b) *a*-MoGe and (e) NbN in the low I_{ac} regime. The red solid line is the fit to $\tilde{\alpha}$ in the low I_{ac} regime, which is extrapolated for $I_{ac} \approx 0$, to obtain α_0 . The magnetic field variation of α_0 for (c) *a*-MoGe and (f) NbN respectively. The black solid circles correspond to α_0 estimated from the linear extrapolation of $\tilde{\alpha}$ for $I_{ac} \approx 0$. The red solid circles correspond to α_0 obtained using the GR model in ref. [16]. The blue solid circles correspond to α_0 used as a parameter for fitting $M'(M'')$ vs I_{ac} under the effect of flux creep.

we obtain $\tilde{\alpha}$. Figs. 9 (a) and (d) show that for the *a*-MoGe and NbN thin films $\tilde{\alpha}$ decreases rapidly with I_{ac} . To estimate α_0 (defined in the limit $I_{ac} \approx 0$), for we plot $\tilde{\alpha} - I_{ac}$ in log-linear scale and linearly extrapolate the value for $I_{ac} \approx 0$. At low I_{ac} , $\tilde{\alpha}$ decreases more rapidly for *a*-MoGe (fig. 9 (b)) than for NbN (fig. 9 (e)). This can be understood from the difference in J_c in the two samples: in *a*-MoGe, which is more weakly pinned than NbN, J_c is two orders of magnitude smaller than NbN and hence the effect of flux creep is stronger. In fig. 9 (c), for *a*-MoGe, we plot together this extrapolated value of $\tilde{\alpha}$ for $I_{ac} \approx 0$ at different magnetic fields (black solid circles) along with α_0 obtained from the full creep analysis (blue solid circles). These two values are very close to each other, whereas the value obtained by neglecting flux creep from the GR analysis is much smaller. In the strongly pinned NbN film (fig. 9 (f)), α_0 estimated from extrapolating $I_{ac} \approx 0$ and that obtained using the GR analysis, are very close to each other. This method outlined above provides a simple scheme to obtain α_0 without doing the complete analysis involving creep.

Quantitatively, the effect on $\tilde{\alpha}$ when creep is neglected can be understood as follows. Flux creep results in a renormalization of α with $|J_{ac}|$, where $\tilde{\alpha}$ is given by,

$$\tilde{\alpha}(J_{ac}) \sim \alpha(J_{ac}) \times \left(\frac{1-\epsilon}{1+\left(\frac{\epsilon}{\omega\tau_0}\right)^2} \right) \quad (13)$$

The calculation of this expression follows from eqn. (12) and is given in details in Appendix C. The first factor on the right hand side, $\alpha(J_{ac})$ contains direct effect of $|J_{ac}|$ on α due to shift of the equilibrium position of the vortex in the pinning potential U , under a drive (eqn. (10)). There is a second correction that is encapsulated in the second factor. The numerator of the second factor, has ϵ (eqn. 5 (a)) which is a measure of the attenuation of U , through the effect of flux creep (eqn. (7)). For small values of J_c , the increase of ϵ is much more rapid with increasing $|J_{ac}|$ and hence the effect of flux creep is more conspicuous in weakly pinned

systems. At low $|J_{ac}|$, ϵ is ~ 0.03 for a -MoGe at 1 kOe , and ~ 0.002 for NbN at 10 kOe , implying that in the weakly pinned a -MoGe, effect of flux creep manifested through the attenuation of U , is stronger than in NbN. However, more significant effect comes from the denominator. The denominator $1 + \left(\frac{\epsilon}{\omega\tau_0}\right)^2$, can be taken ~ 1 if $\omega \gg \tau_0^{-1}$. This happens when the probing frequency is sufficiently high. In our case we are in the low frequency regime (tens of kHz). τ_0 (eqn. 5 (b)) which is given by η/α , is large enough such that $\omega\tau_0 \leq 1$. For a -MoGe at 1 kOe , $\omega\tau_0$ ranges from $0.038 - 0.004$, with increasing $|J_{ac}|$ such that $\left(\frac{\epsilon}{\omega\tau_0}\right)^2 \sim 0.6 - 1700$. In the case of NbN, $\omega\tau_0$ varies from 0.01 till 0.0007 , which in turn makes $\left(\frac{\epsilon}{\omega\tau_0}\right)^2$ vary from ~ 0.04 till 950 at 10 kOe . Therefore, even if $\epsilon \ll 1$, $\tilde{\alpha}$ scales as $\left(\frac{\epsilon}{\omega\tau_0}\right)^{-2}$, which makes $\tilde{\alpha} \ll \alpha$ particularly at high $|J_{ac}|$.

6. Conclusion

We have shown that flux creep can give rise to strong nonlinearity in the electrodynamic response in the vortex state of superconducting thin films that extends down to very low ac excitations. The non-linear vortex response, which in our experiment is embedded in the variation of M with I_{ac} can be described by combining the effect of flux creep with the model developed by Coffey and Clem³⁵. Our results lend support to the suggestion that at subcritical currents the vortex viscosity is exponentially larger than the Bardeen-Stephen estimate (eqn. (11)) even though its microscopic origin needs to be investigated further. It is important to note that this nonlinearity extends to magnetic fields where the magnetisation vs. magnetic field curve has closed and therefore the superconductor has no apparent irreversibility. Neglecting flux creep when analysing the data can result in underestimating the Labusch parameter, α , particularly in weakly pinned thin films, where the effect of creep is

more important. In addition, we have also presented a simple extrapolation scheme to obtain the correct value α from the non-linear ac response.

Although our analysis can capture the variation of M vs. I_{ac} within reasonable accuracy, some outstanding questions remain. First, in NbN the weak variation of M' at small I_{ac} could not be captured with any of the existing models of flux creep. Secondly, our analysis overestimates the magnitude M'' compared to experiments. These discrepancies point to the limitations of existing theoretical models and need to be addressed in future studies.

7. Acknowledgement

This work was financially supported by Department of Atomic Energy, Government of India. We thank Ganesh Jangam for help with magnetisation measurements.

8. Author Contribution

SB performed the ac shielding response measurements and analysed the data. Sample growth and basic characterisation was done by SB, SM, VB and JJ. PR conceived the problem and supervised the project. The paper was written by SB and PR. All authors commented on the manuscript.

Appendix A

1) Calculation of $J_{ac}(r)$ and $\tilde{\lambda}(r)$ considering effect of flux creep

The induced current density in the superconducting film, $J_{ac}(r)$, is obtained by solving the coupled Maxwell's and London equation for the geometry of our system, and is given by the following self-consistent equations,

$$\mathbf{A}_{film}(\mathbf{r}) = \mathbf{A}_{drive}(\mathbf{r}) + \frac{\mu_0}{4\pi} \int d^3\mathbf{r}' \frac{J_{ac}(\mathbf{r}')}{|\mathbf{r}-\mathbf{r}'|} \quad (14)$$

$$\mathbf{A}_{film}(\mathbf{r}) = -\mu_0 \tilde{\lambda}^2 J_{ac}(\mathbf{r}) \quad (15)$$

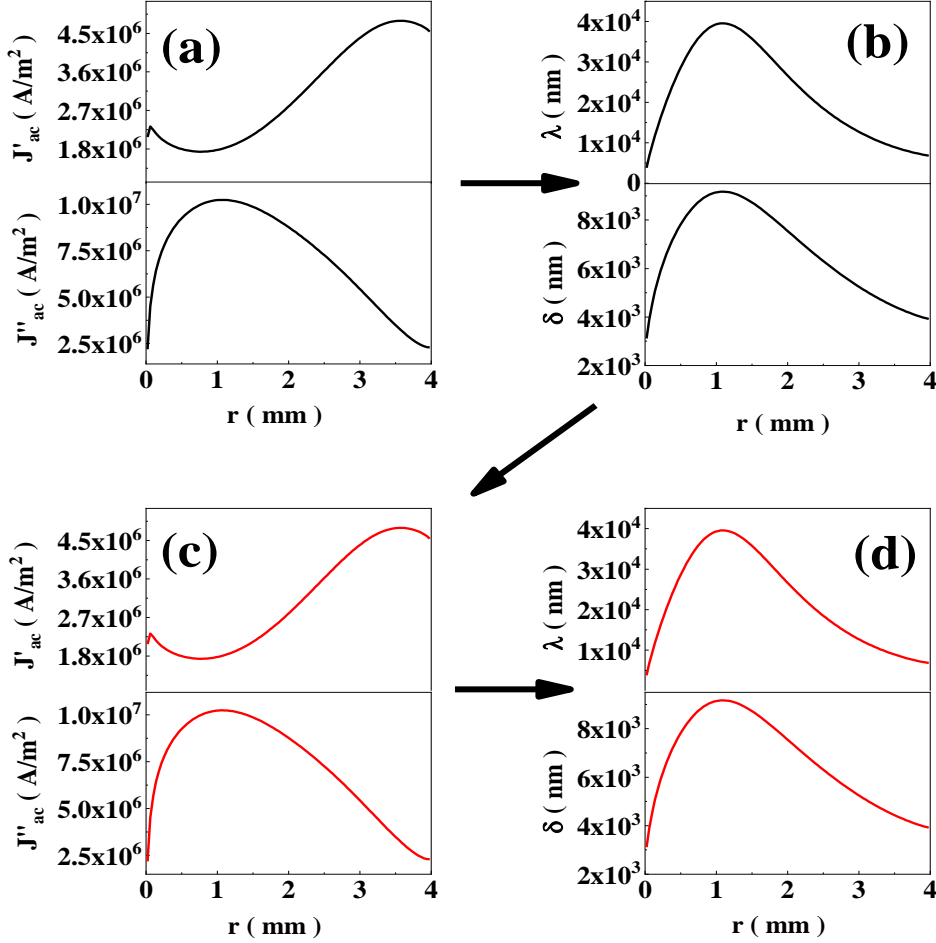


Figure 10. Radial variation of J'_{ac} , J''_{ac} , and λ , δ at $I_{ac} = 2$ mA. The profile of J'_{ac} (J''_{ac}) in (a) is used to calculate λ (δ) in (b), which in turn is used to calculate the profile of J'_{ac} (J''_{ac}) in (c). The profile of λ (δ) in (d) is obtained using J'_{ac} (J''_{ac}) in (c). The black and red solid lines correspond to the 1st and 2nd iterations respectively of the self-consistency check procedure. We have taken $\alpha_0 \sim 46$ Nm⁻², $\frac{U_0}{k_B} \sim 13.2$ K and $J_c \sim 4.8 \times 10^7$ Am⁻² along with $\eta = \eta_{BS} e^{U_0/k_B T}$ where $\eta_{BS} \sim 1.47 \times 10^{-8}$ Nsm⁻² at $T = 2$ K and $B = 1$ kOe.

where $\mathbf{A}_{film}(\mathbf{r})$ is the vector potential of the superconducting film. It is a combination of the vector potential associated with the primary coil, $\mathbf{A}_{drive}(\mathbf{r})$, due to passage of an ac current through it, and the induced current density, J_{ac} , on the superconducting film and $\tilde{\lambda}$ is the

complex penetration depth. The scheme for numerically solving these equations for a circular geometry and a constant $\tilde{\lambda}$ and obtaining $M'(M'')$, is given in refs. [11] and [12].

When the effect of flux creep is included, additional complications arise when $\tilde{\lambda}$ becomes a function of the induced current density J_{ac} which is function of the radial distance from the center of the film r . The relation between $J_{ac}(r)$ and $\tilde{\lambda}$, can be calculated using eqns. (7), (10), (11) and (12). To obtain a self-consistent solution between $J_{ac}(r)$ and $\tilde{\lambda}$, we adopt an iterative procedure. In the first step, assume constant values for α_0 , $\frac{U_0}{k_B}$ and $\eta \sim \eta_{BS} e^{\frac{U_0}{k_B T}}$ and calculate $J_{ac}(r)$ using eqns. (14) and (15). In the second step, we use the calculated $J_{ac}(r)$ in the first step and calculate $\tilde{\lambda}(r)$ using eqns. (7), (10), (11) and (12) and calculate $J_{ac}(r)$ using this modified $\tilde{\lambda}(r)$. This procedure is then repeated till a convergence is reached.

While this basic procedure leads to a convergence at low values of I_{ac} , as I_{ac} is increased, this iteration fails to converge. We therefore modify the protocol in the following way. From the 7th iteration step we take the average of the $\tilde{\lambda}(r)$ in the last 6 iterations to calculate $J_{ac}(r)$. This protocol converges up to the maximum I_{ac} in about 300 iterations.

To cross-check the self-consistency of the procedure, we use the final $J_{ac}(r)$ obtained after convergence and use it to directly compute $\tilde{\lambda}(r)$, using eqns. (7), (10), (11) and (12). Next, using the computed value of $\tilde{\lambda}(r)$, we recalculate $J_{ac}(r)$ using eqns. (14) and (15) and verify that we get the same result. This is shown in fig. (10) for *a*-MoGe at $B = 1 \text{ kOe}$ at $I_{ac} = 2 \text{ mA}$.

Appendix B

Complete dataset of *a*-MoGe and NbN for the fits to the electromagnetic shielding response as a function of I_{ac} at different DC magnetic fields

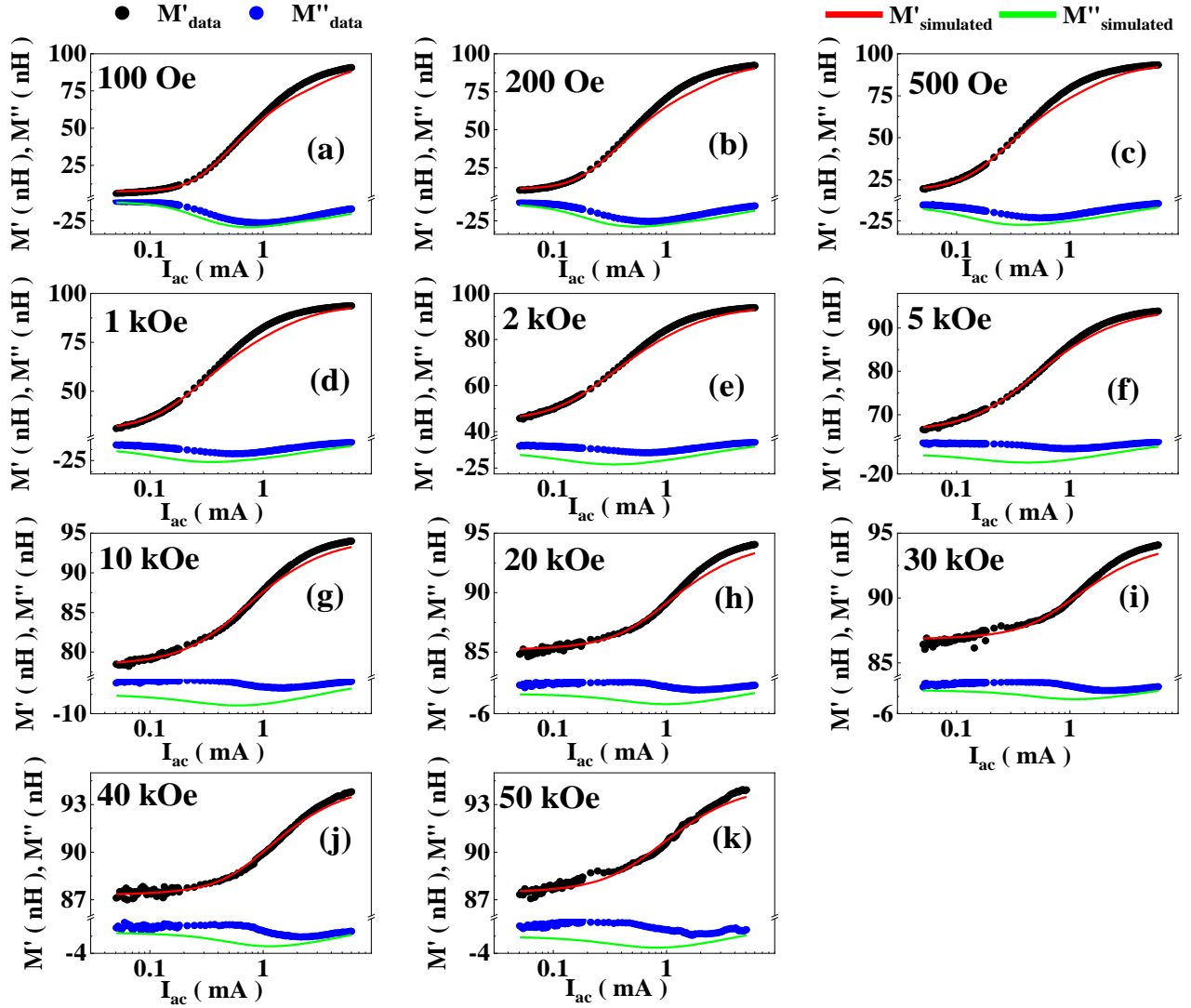


Figure 11. (a) – (k) I_{ac} dependence of M' and M'' of 20 nm *a*-MoGe at different applied DC magnetic fields. The black and blue solid circles are the experimentally measured M' and M'' respectively while the red and green solid lines are the fits to M' and M'' . The measurements are done at $T = 2 K$ and $f = 30 kHz$.

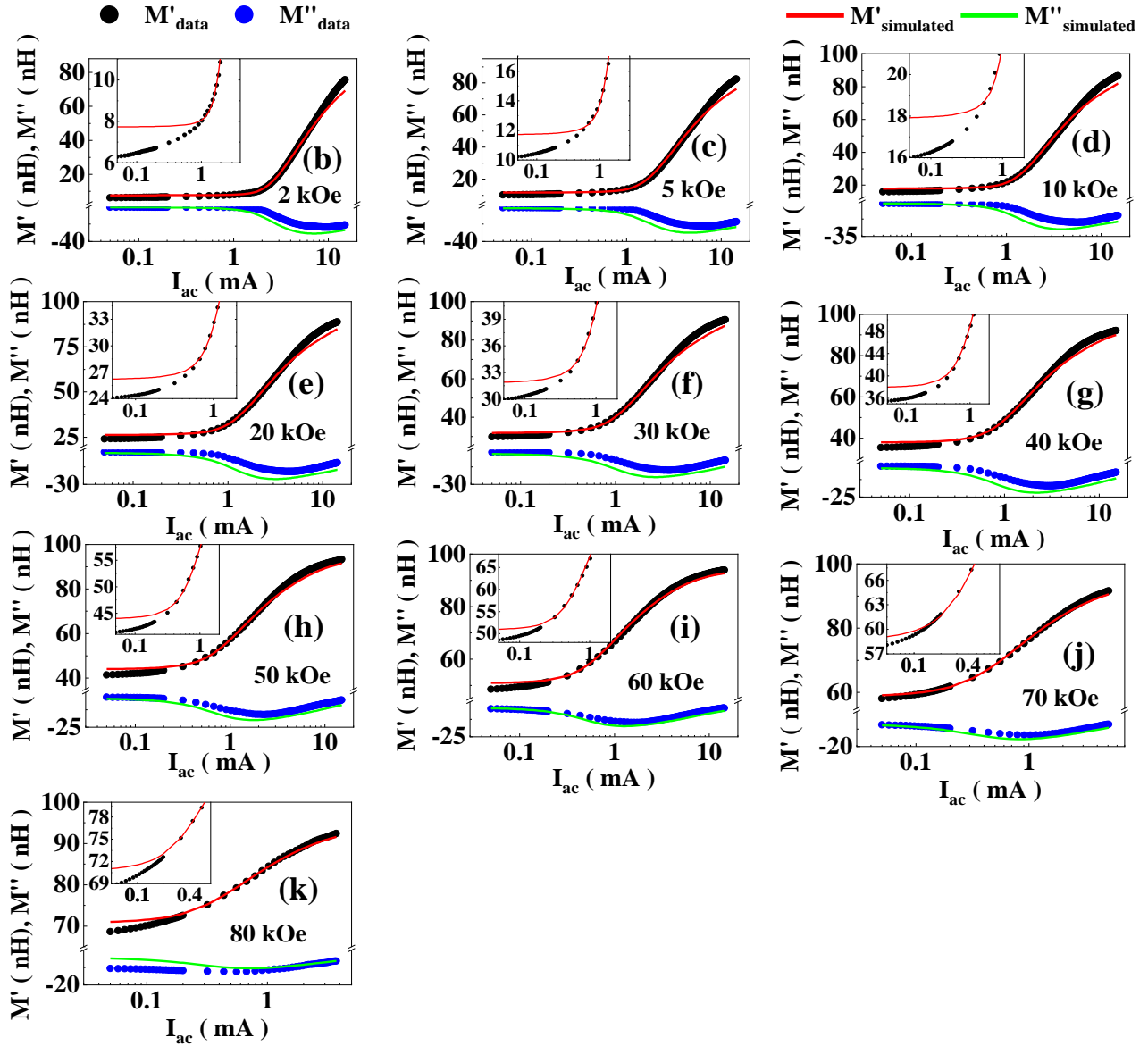


Figure 12. (a) – (k) I_{ac} dependence of M' and M'' of 5 nm NbN at different applied DC magnetic fields. The black and blue solid circles are the experimentally measured M' and M'' respectively while the red and green solid lines are the fits to M' and M'' . The insets (X-axis in mA and Y-axis in nH) show the deviation of the fit to M' from the experimental data at low I_{ac} . The measurements are done at $T = 2$ K and $f = 30$ kHz.

Appendix C

Calculation of α_L and η under the influence of flux creep

We have the CC eqn. (12) which is : $\tilde{\lambda}^{-2} = \lambda^{-2} + i\delta^{-2} = \left(\lambda_L^2 - i \frac{\rho_{ff} \epsilon + i\omega\tau}{\mu_0\omega 1 + i\omega\tau} \right)^{-1}$ where $\epsilon = \frac{1}{I_0^2(\nu)}$ and $\tau = \tau_0 \frac{I_0^2(\nu) - 1}{I_1(\nu)I_0(\nu)}$ (eqn. (5)) and $\tau_0 = \eta/\alpha$. In our analysis, $\frac{I_0^2(\nu) - 1}{I_1(\nu)I_0(\nu)} \sim 1.15 - 1.18$ and hence for simplicity in the calculations to follow, we assume $\tau \sim \tau_0$. Eqn. (12) can be simplified as follows:

$$\begin{aligned} \tilde{\lambda}^2 &\sim \lambda_L^2 - i \frac{\rho_{ff} \epsilon + i\omega\tau_0}{\mu_0\omega 1 + i\omega\tau_0} \\ \Rightarrow \tilde{\lambda}^2 - \lambda_L^2 &\sim \frac{\rho_{ff} \omega\tau_0 - i\epsilon}{\mu_0\omega 1 + i\omega\tau_0} \\ \Rightarrow \tilde{\lambda}^2 - \lambda_L^2 &\sim \frac{B\phi_0 \omega\tau_0 - i\epsilon}{\mu_0\omega\eta 1 + i\omega\tau_0} \\ \Rightarrow (\tilde{\lambda}^2 - \lambda_L^2)^{-1} &\sim \frac{\mu_0\omega\eta}{B\phi_0} (1 + i\omega\tau_0)(\omega\tau_0 - i\epsilon)^{-1} \\ \Rightarrow (\tilde{\lambda}^2 - \lambda_L^2)^{-1} &\sim \frac{\mu_0\eta}{B\phi_0\tau_0} (1 + i\omega\tau_0) \left(1 - \frac{i\epsilon}{\omega\tau_0}\right)^{-1} \\ \Rightarrow (\tilde{\lambda}^2 - \lambda_L^2)^{-1} &\sim \frac{\mu_0\alpha}{B\phi_0} (1 + i\omega\tau_0) \left(1 - \frac{i\epsilon}{\omega\tau_0}\right)^{-1} \\ \Rightarrow (\tilde{\lambda}^2 - \lambda_L^2)^{-1} &\sim \frac{\mu_0}{B\phi_0} (\alpha + i\omega\eta) \left(1 - \frac{i\epsilon}{\omega\tau_0}\right)^{-1} \\ \Rightarrow (\tilde{\lambda}^2 - \lambda_L^2)^{-1} &\sim \frac{\mu_0}{B\phi_0} \frac{(\alpha + i\omega\eta)}{\left(1 - \frac{i\epsilon}{\omega\tau_0}\right)} \end{aligned}$$

$$\begin{aligned}
&\Rightarrow (\tilde{\lambda}^2 - \lambda_L^2)^{-1} \sim \frac{\mu_0}{B\phi_0} \frac{(\alpha + i\omega\eta)}{1 + \left(\frac{\epsilon}{\omega\tau_0}\right)^2} \left(1 + \frac{i\epsilon}{\omega\tau_0}\right) \\
&\Rightarrow (\tilde{\lambda}^2 - \lambda_L^2)^{-1} \sim \frac{\mu_0}{B\phi_0} \frac{1}{1 + \left(\frac{\epsilon}{\omega\tau_0}\right)^2} \left(\alpha + \frac{i\epsilon\alpha^2}{\omega\eta} + i\omega\eta - \alpha\epsilon\right) \\
&\Rightarrow (\tilde{\lambda}^2 - \lambda_L^2)^{-1} \sim \frac{\mu_0}{B\phi_0} \frac{1}{1 + \left(\frac{\epsilon}{\omega\tau_0}\right)^2} \left(\alpha(1 - \epsilon) + i\omega\eta \left(1 + \epsilon \left(\frac{1}{\omega\tau_0}\right)^2\right)\right) \\
&\Rightarrow (\tilde{\lambda}^2 - \lambda_L^2)^{-1} \sim \frac{\mu_0}{B\phi_0} (\tilde{\alpha} + i\omega\tilde{\eta}) \quad (16)
\end{aligned}$$

where $\tilde{\alpha}$ and $\tilde{\eta}$ are the pinning force constant and vortex viscosity, renormalized due to the effect of flux creep. These quantities are related to their creep free counterparts as:

$$\tilde{\alpha} \sim \alpha \frac{(1-\epsilon)}{1 + \left(\frac{\epsilon}{\omega\tau_0}\right)^2} \quad (17 \text{ (a)})$$

$$\tilde{\eta} \sim \eta \frac{\left(1 + \epsilon \left(\frac{1}{\omega\tau_0}\right)^2\right)}{1 + \left(\frac{\epsilon}{\omega\tau_0}\right)^2} \quad (17 \text{ (b)})$$

-
- ¹ Abrikosov A A 1957 The magnetic properties of superconducting alloys *J. Phys. Chem. Solids* **2** 199
- ² Bardeen J and Stephen M J 1965 Theory of the Motion of Vortices in Superconductors *Phys. Rev.* **140** A1197
- ³ Schmidt V V and Balkov A A 1970 Critical current in superconducting films *Sov. Phys. JETP* **30** 1137
- ⁴ Eley S, Glatz A, and Willa R 2021 Challenges and transformative opportunities in superconductor vortex physics, *J. Appl. Phys.* **130** 050901
- ⁵ Fomin V M and Dobrovolskiy O V 2022 A Perspective on superconductivity in curved 3D nanoarchitectures *Appl. Phys. Lett.* **120** 090501
- ⁶ Naibert T R, Polshyn H, Garrido-Menacho R, Durkin M, Wolin B, Chua V, Mondragon-Shem I, Hughes T, Mason N and Budakian R 2021 Imaging and controlling vortex dynamics in mesoscopic superconductor–normal-metal–superconductor arrays *Phys. Rev. B* **103** 224526
- ⁷ Chaves D A D, de Araújo I M, Carmo D, Colauto F, de Oliveira A A M, de Andrade A M H, Johansen T H, Silhanek A V, Ortiz W A and Motta M 2021 Enhancing the effective critical current density in a Nb superconducting thin film by cooling in an inhomogeneous magnetic field *Appl. Phys. Lett.* **119** 022602
- ⁸ Li W, Reichhardt C J O, Jankó B, and Reichhardt C 2021 Vortex dynamics, pinning, and angle-dependent motion on moiré patterns *Phys. Rev. B* **104** 024504
- ⁹ Sang L N, Li Z, Yang G S, Yue Z J, Liu J X, Cai C B, Wu T, Dou S X, Ma Y W and Wang X L 2021 Pressure effects on iron-based superconductor families: Superconductivity, flux pinning and vortex dynamics *Mater. Today Phys.* **19** 100414
- ¹⁰ Turneaure S J, Ulm E R and Lemberger T R 1996 Numerical modeling of a two-coil apparatus for measuring the magnetic penetration depth in superconducting films and arrays *J. Appl. Phys.* **79** 4221
- ¹¹ Turneaure S J, Pesetski A A and Lemberger T R 1998 Numerical modeling and experimental considerations for a two-coil apparatus to measure the complex conductivity of superconducting films *J. Appl. Phys.* **83** 4334
- ¹² Mondal M 2013 Phase fluctuations in a conventional s-wave superconductor: Role of dimensionality and disorder *arXiv:1303.7396v2*
- ¹³ Kumar S, Kumar C, Jesudasan J, Bagwe V, Raychaudhuri P and Bose S 2013 A two-coil mutual inductance technique to study matching effect in disordered NbN thin films *Appl. Phys. Lett.* **103** 262601
- ¹⁴ Gupta C, Parab P and S. Bose 2020 Superfluid density from magnetic penetration depth measurements in Nb–Cu 3D nano-composite films *Sci. Rep.* **10** 18331
- ¹⁵ Fiory A T, Hebard A F and Glaberson W I 1983 Superconducting phase transitions in indium/indium-oxide thin-film composites *Phys. Rev. B* **28** 5075
- ¹⁶ Basistha S, Mandal S, Jesudasan J, Bagwe V and Raychaudhuri P 2024 Low-frequency electrodynamics in the mixed state of superconducting NbN and *a*-MoGe films using two-coil mutual inductance technique *Supercond. Sci. Technol.* **37** 085027

-
- ¹⁷ Vinokur V M, Geshkenbein V B, Feigel'man M V and Blatter G 1993 Scaling of the Hall Resistivity in high- T_c superconductors *Phys. Rev. Lett.* **71** 1242
- ¹⁸ Carruzzo H M and Yu C C 2000 Viscoelasticity and surface tension at the defect-induced first-order melting transition of a vortex lattice *Phys. Rev. B* **61** 1521
- ¹⁹ Pashinsky B V, Feigel'man M V and Andreev A V 2023 Microwave response of type-II superconductors at weak pinning *SciPost Phys.* **14** 096
- ²⁰ de Lima O F and Cardoso C A 2000 Experimental study of scaling laws for the complex susceptibility of type-II superconductors *Phys. Rev. B* **61** 11722
- ²¹ Raedts S, Silhanek A V, Moshchikov V V, Moonens J and Leunissen H A 2006 Crossover from intravalley to intervalley vortex motion in type-II superconductors with a periodic pinning array *Phys. Rev. B* **73** 174514
- ²² Li X F, Grivel J C, Abrahamsen A B and Andersen N H 2012 Critical current density measurement of thin films by AC susceptibility based on the penetration parameter h *Physica C* **477** 6
- ²³ Pasquini G, Civale L, Lanza H and Nieva G 1999 Dynamic regimes in the ac response of $\text{YBa}_2\text{Cu}_3\text{O}_7$ with columnar defects: Intra- and inter-valley vortex motion *Phys. Rev. B* **59** 9627
- ²⁴ Galluzzi A, Buchkov K, Tomov V, Nazarova E, Leo A, Grimaldi G, Pace S and Polichetti M 2020 Mixed state properties analysis in AC magnetic field of strong pinning Fe(Se,Te) single crystal *Supercond. Sci. Technol.* **33** 094006
- ²⁵ Clem J R and Sanchez A 1994 Hysteretic ac losses and susceptibility of thin superconducting disk *Phys. Rev. B* **50** 9355
- ²⁶ Brandt E H 1998 Superconductor disks and cylinders in an axial magnetic field: II. Nonlinear and linear ac susceptibilities *Phys. Rev. B* **58** 6523
- ²⁷ Gittleman J I and Rosenblum B 1966 Radio-Frequency Resistance in the Mixed State for Subcritical Currents *Phys. Rev. Lett.* **16** 734
- ²⁸ Labusch R 1969 Calculation of the critical field gradient in type-II superconductors *Cryst. Lattice Defects* **1** 1
- ²⁹ van der Beek C J, Geshkenbein V B and Vinokur V M 1993 Linear and nonlinear ac response in the superconducting mixed state *Phys. Rev. B* **48** 3393
- ³⁰ Tinkham M 1996 *Introduction to Superconductivity* 2nd edn. (New York: McGraw-Hill)
- ³¹ London F and London H 1935 The electromagnetic equations of the supraconductor *Proc. R. Soc. A* **149** 71
- ³² Campbell A M 1969 The response of pinned flux vortices to low-frequency fields *J. Phys. C: Solid State Phys.* **2** 1492
- ³³ Campbell A M 1971 The interaction distance between flux lines and pinning centres *J. Phys. C: Solid State Phys.* **4** 3186
- ³⁴ Kim H, Tanatar M A, Hodovanets H, Wang K, Paglione J and Prozorov R 2021 Campbell penetration depth in low carrier density superconductor YPtBi *Phys. Rev. B* **104** 014510

-
- ³⁵ Coffey M W and Clem J R 1991 Unified theory of effects of vortex pinning and flux creep upon the rf surface impedance of type-II superconductors *Phys. Rev. Lett.* **67** 386
- ³⁶ Fulde P, Pietronero L, Schneider W R and Strässler S 1975 Problem of Brownian Motion in a Periodic Potential *Phys. Rev. Lett.* **35** 1776
- ³⁷ Dieterich W, Peschel I and Schneider W R 1977 Diffusion in periodic potentials *Z. Physik B* **27** 177
- ³⁸ Pompeo N and Silva E 2008 Reliable determination of vortex parameters from measurements of the microwave complex resistivity *Phys. Rev. B* **78** 094503
- ³⁹ Kim Y B, Hempstead C F and Strand A 1962 Critical persistent currents in hard superconductors *Phys. Rev. Lett.* **9** 306
- ⁴⁰ Anderson P W and Kim Y B 1964 Hard Superconductivity: Theory of the Motion of Abrikosov Flux Lines *Rev. Mod. Phys.* **36** 39
- ⁴¹ Beasley M R, Labusch R and Webb W W 1969 Flux Creep in Type-II Superconductors *Phys. Rev.* **181** 682
- ⁴² Griessen R 1991 Thermally activated flux motion near the absolute zero *Physica C* **172** 441
- ⁴³ Lairson B M, Sun J Z, Geballe T H, Beasley M R and Bravman J C 1991 Thermal activation of vortex motion in $\text{YBa}_2\text{Cu}_3\text{O}_{7-\delta}$ films at low temperatures *Phys. Rev. B* **43** 10405
- ⁴⁴ Feigel'man, M V, Geshkenbein V B, Larkin A I and Vinokur V M 1989, Theory of collective flux creep *Phys. Rev. Lett.* **63** 2303
- ⁴⁵ Feigel'man M V, Geshkenbein V B and Vinokur V M 1991 Flux creep and current relaxation in high- T_c superconductors *Phys. Rev. B* **43**, 6263
- ⁴⁶ Zeldov E, Amer N M, Koren G, Gupta A, McElfresh M W and Gambino R J 1990 Flux creep characteristics in high-temperature superconductors *Appl. Phys. Lett.* **56** 680
- ⁴⁷ Zeldov E, Amer N M, Koren G and Gupta A 1990 Flux creep in $\text{Bi}_2\text{Sr}_2\text{CaCu}_2\text{O}_8$ epitaxial films *Appl. Phys. Lett.* **56** 1700
- ⁴⁸ Prozorov R, Giannetta R W, Kameda N, Tamegai T, Schlueter J A and Fournier P 2003 Campbell penetration depth of a superconductor in the critical state *Phys. Rev. B* **67** 184501
- ⁴⁹ Chockalingam S P, Chand M, Jesudasan J, Tripathi V and Raychaudhuri P 2008 Superconducting properties and Hall effect of epitaxial NbN thin films *Phys. Rev. B* **77** 214503
- ⁵⁰ Kamlapure A, Mondal M, Chand M, Mishra A, Jesudasan J, Bagwe V, Benfatto L, Tripathi V and Raychaudhuri P 2010 Measurement of magnetic penetration depth and superconducting energy gap in very thin epitaxial NbN films *Appl. Phys. Lett.* **96** 072509
- ⁵¹ Roy I, Dutta S, Roy Choudury A N, Basistha S, Maccari I, Mandal S, Jesudasan J, Bagwe V, Castellani C, Benfatto L and Raychaudhuri P 2019 Melting of the Vortex Lattice through Intermediate Hexatic Fluid in an a-MoGe Thin Film *Phys. Rev. Lett.* **122** 047001
- ⁵² Bean C P and Livingston J D 1964 Surface Barrier in Type-II Superconductors *Phys. Rev. Lett.* **12**

-
- ⁵³ Zeldov E, Larkin A I, Geshkenbein V B, Konczykowski M, Majer D, Khaykovich B, Vinokur V M and Shtrikman H 1994 Geometric Barriers in High-Temperature Superconductors *Phys. Rev. Lett.* **73** 1428
- ⁵⁴ Pissas M and Stamopoulos D 2001 Evidence for geometrical barriers in an untwinned $\text{YBa}_2\text{Cu}_3\text{O}_{7-\delta}$ single crystal *Phys. Rev. B* **64** 134510
- ⁵⁵ Nuragliev T 1995 Theoretical study of superconducting film response to AC magnetic field *Physica C* **249** 25
- ⁵⁶ Nurgaliev T 2002 Current distribution in HTS thin films induced by inhomogeneous magnetic field *AIP Conf. Proc.* **614** 452
- ⁵⁷ Buchachek M, Xiao Z L, Dutta S, Andrei E Y, Raychaudhuri P, Geshkenbein V B and Blatter G 2019 Experimental test of strong pinning and creep in current-voltage characteristics of type-II superconductors *Phys. Rev. B* **100** 224502
- ⁵⁸ Dutta S, Roy I, Basistha S, Mandal S, Jesudasan J, Bagwe V and Raychaudhuri P 2020 Collective flux pinning in hexatic vortex fluid in *a*-MoGe thin film *J. Phys.: Condens. Matter* **32** 075601
- ⁵⁹ Kundu H K, Amin K R, Jesudasan J, Raychaudhuri P, Mukherjee S and Bid A 2019 Effect of dimensionality on the vortex dynamics in a type-II superconductor *Phys. Rev. B* **100** 174501
- ⁶⁰ Gvaler J R, Janocko M A, Patterson A and Jones C K 1971 Very High Critical Current and Field Characteristics of Niobium Nitride Thin Films *J. Appl. Phys.* **42** 54